



OPEN

Inoculation of silicon nanoparticles with silver atoms

SUBJECT AREAS:

SYNTHESIS AND
PROCESSING

NANOPARTICLES

Cathal Cassidy¹, Vidyadhar Singh¹, Panagiotis Grammatikopoulos¹, Flyura Djurabekova², Kai Nordlund² & Mukhles Sowwan^{1,3}¹Nanoparticles by Design Unit, Okinawa Institute of Science and Technology (OIST) Graduate University, 1919-1 Onna-Son, Okinawa, 904-0495, Japan, ²Department of Physics and Helsinki Institute of Physics, University of Helsinki, P.O. Box 43, FIN-00014 Helsinki, Finland, ³Nanotechnology Research Laboratory, Al-Quds University, East Jerusalem, P.O. Box 51000, Palestine.Received
29 July 2013Accepted
14 October 2013Published
30 October 2013Correspondence and
requests for materials
should be addressed to
M.S. (mukhles@oist.jp)

Silicon (Si) nanoparticles were coated inflight with silver (Ag) atoms using a novel method to prepare multicomponent heterostructured metal-semiconductor nanoparticles. Molecular dynamics (MD) computer simulations were employed, supported by high-resolution bright field (BF) transmission electron microscopy (HRTEM) and aberration-corrected scanning transmission electron microscopy (STEM) with a resolution ≤ 0.1 nm in high angle annular dark field (HAADF) mode. These studies revealed that the alloying behavior and phase dynamics during the coating process are more complex than when attaching hetero-atoms to preformed nanoparticles. According to the MD simulations, Ag atoms condense, nucleate and diffuse into the liquid Si nanoparticles in a process that we term “inoculation”, and a phase transition begins. Subsequent solidification involves an intermediate alloying stage that enabled us to control the microstructure and crystallinity of the solidified hybrid heterostructured nanoparticles.

Design and fabrication of multicomponent heterostructured nanoparticles has attracted significant research activity in recent years, targeting a range of different applications^{1–6}. As a result of the interaction at the interface between the different components, these nanoparticles usually possess optical, electronic, and catalytic properties which are not exhibited in their single component counterparts^{4–11}. The required properties can be tailored by tuning the crystallinity and volume fraction of each component, in addition to nanoparticle size. Several chemical and physical methods have been used, with different degrees of success, to grow heterostructured nanoparticles^{1–10}. Of the physical techniques, magnetron-sputter inert-gas aggregation has emerged as one of the most prevalent and flexible techniques because it is possible to control the growth process by varying parameters such as the magnetron power, the aggregation length, and the inert gas pressure^{12–17}.

In this work, we investigated experimentally and with MD computer simulations the coating process of freshly nucleated Si nanoparticles with Ag atoms to prepare multicomponent heterostructured metal-semiconductor nanoparticles in a controlled way. The Si–Ag system is interesting because Si is photoluminescent while Ag is plasmonic and, most importantly, because Si and Ag are eutectic system-forming materials immiscible in the solid state^{18–27}. In cell biology, the combination of fluorescent and plasmonic materials in a single nanoparticle is attractive for multi-modal bio-imaging, biosensors and 3D optical sectioning^{23–25}. The interplay between fluorescence and plasmonic effects in Ag–Si–SiO₂ has been reported comprehensively by Kalkman et al²⁶, albeit in a hybrid nanoparticle/thin film context, with the finding that the emission efficiency can be enhanced. Similarly, there is also significant potential for enhancement of the efficiency of solar cells by inclusion of hybrid Si/Ag nanoparticles²⁷. Considering nanoparticle functionalization, which is essential for successful real-world applications like drug delivery and cancer therapy, a well-controlled hybrid nanostructure offers simultaneous bio-conjugation of different moieties (e.g. DNA, antibodies, peptides) with the different surface chemistries of Si and Ag²⁸.

Nanoparticles were produced using a modified inert-gas aggregated magnetron sputtering system (Fig. 1). The principles of particle formation in magnetron sputtering with inert-gas aggregation are well established^{12–17}. In our experiments, a supersaturated Si vapor was generated by DC magnetron sputtering of a high-purity Si target mounted in a water-cooled aggregation chamber (Fig. 1, labeled ‘I’). Within this aggregation zone, nucleation of Si clusters took place in an inert gas atmosphere at relatively high pressure (see Methods), and was followed by the nucleation and growth of larger Si nanoparticles due to coalescence. The pressure difference between the (high pressure) aggregation zone and the (low pressure) sample deposition chamber (Fig. 1, labeled ‘III’) transported the freshly nucleated Si nanoparticles through the differential-pumping orifice and out of the aggregation zone.

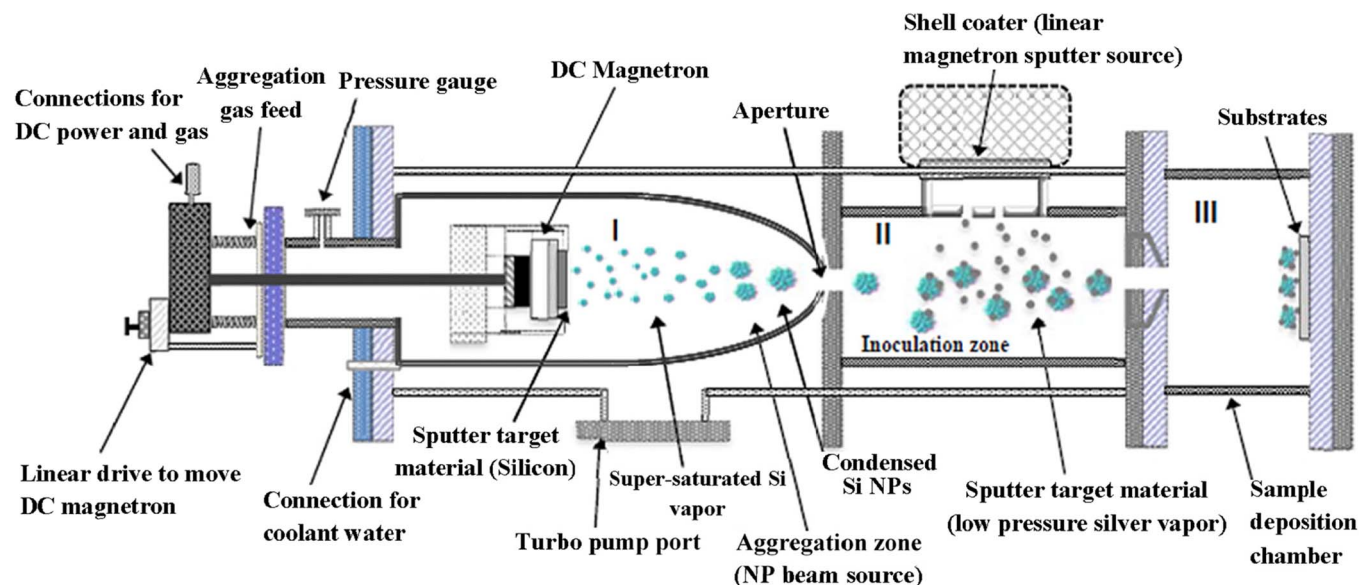


Figure 1 | Schematic drawing of the modified magnetron-sputter inert-gas condensation system. The system consists of three zones: I- the Si nanoparticle growth zone, II- the Ag coating zone, and III- the sample deposition zone.

Without further intervention, uncoated Si would ultimately cool and vitrify into solid, amorphous Si as was observed in control samples. However, as the central focus of this work, we applied an incident flux of Ag atoms to coat the Si nanoparticles as they exited the aggregation zone through the orifice. Ag was sputtered from a linear magnetron sputter target in the coating zone (Fig. 1, labeled 'II'), positioned parallel to the flight direction of the Si nanoparticles, en route from aggregation zone chamber to sample deposition chamber.

Results

Morphology and structure of Ag-coated Si nanoparticles. After substrate landing, nanoparticle-loaded substrates were load-lock transferred to an inert gas glovebox and scanned with atomic force microscopy (AFM), as shown in Fig. 2a and 2b. The height distribution was well approximated by a log-normal function (red curve), having an average height of 12.5 nm and FWHM of 4.7 nm. An overview Z-contrast HAADF STEM micrograph reveals a distinctive structure: multiple Ag nanoclusters on the surface of each Si nanoparticle (Fig. 2c). Chemical composition of hybrid nanoparticles was confirmed by energy dispersive X-ray spectroscopy (EDS) (Supplementary Information, Fig. S1a). The

average diameter of the nanoparticles, estimated from the low-magnification TEM images (Fig. S1b-S1e presented in the Supplementary Information), is consistent with the AFM results of Fig. 2a and 2b. TEM tilt series characterization (Supplementary Information, Fig. S2a, 2b and 2c), showed that the Ag nanoclusters were on the Si surface and not embedded in the Si core.

HRTEM imaging revealed that control Si nanoparticles, which were not exposed to Ag vapor, were amorphous (Fig. 3a, and FFT pattern presented in the Supplementary Information, Fig. S3). In contrast, Ag-coated Si nanoparticles were nanocrystalline. For example, Fig. 3b is a high resolution HAADF-STEM micrograph of one ~ 13 nm hybrid nanoparticle decorated by four Ag nanoclusters of diameter ~ 3 nm (indicated by numerals 1-4) and encapsulated with ~ 2 nm oxide shell. A bright field HRTEM image of the same nanoparticle, with unchanged orientation with respect to the electron beam, is shown in Fig. 3c. The Ag nanoclusters, previously marked by 1-4 in Fig. 3b, appear as dark spots in the bright-field image of Fig. 3c. Both micrographs of Fig. 3b, c indicate that the Si core consists of small grains of different crystallographic orientations²⁹⁻³². In Fig. 3c, the indicated grain (blue arrow) is aligned such that a Si $\langle 110 \rangle$ zone axis is parallel to the electron beam, and the Si $\{111\}$ lattice planes can easily be discerned. Multiple twinning is

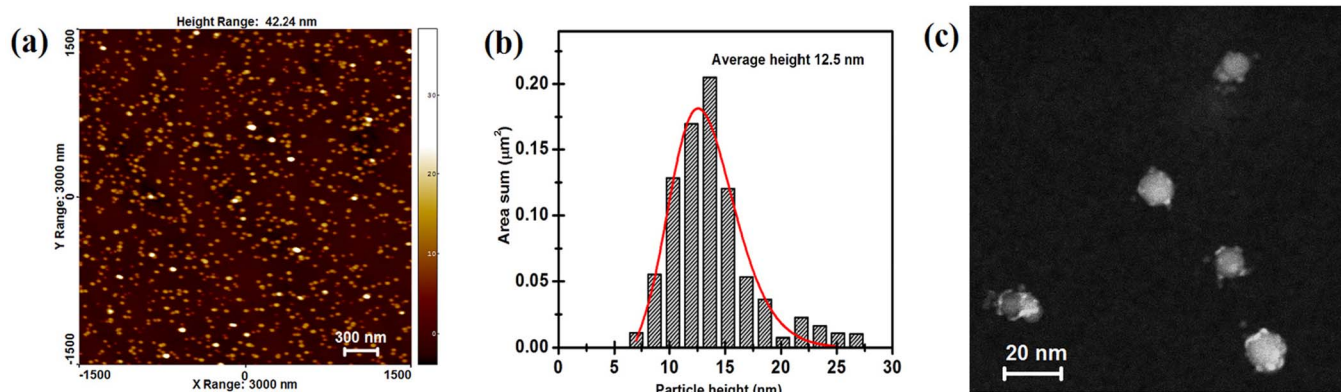


Figure 2 | Size and morphology of the Ag coated Si nanoparticles. (a) AFM topography image of Si core nanoparticles coated with Ag (b) AFM Height distribution histogram of more than 1000 Si-Ag particles, and (c) HAADF-STEM micrograph of Si nanoparticles (gray) decorated with Ag nanoclusters (white), on a thin carbon substrate (black).

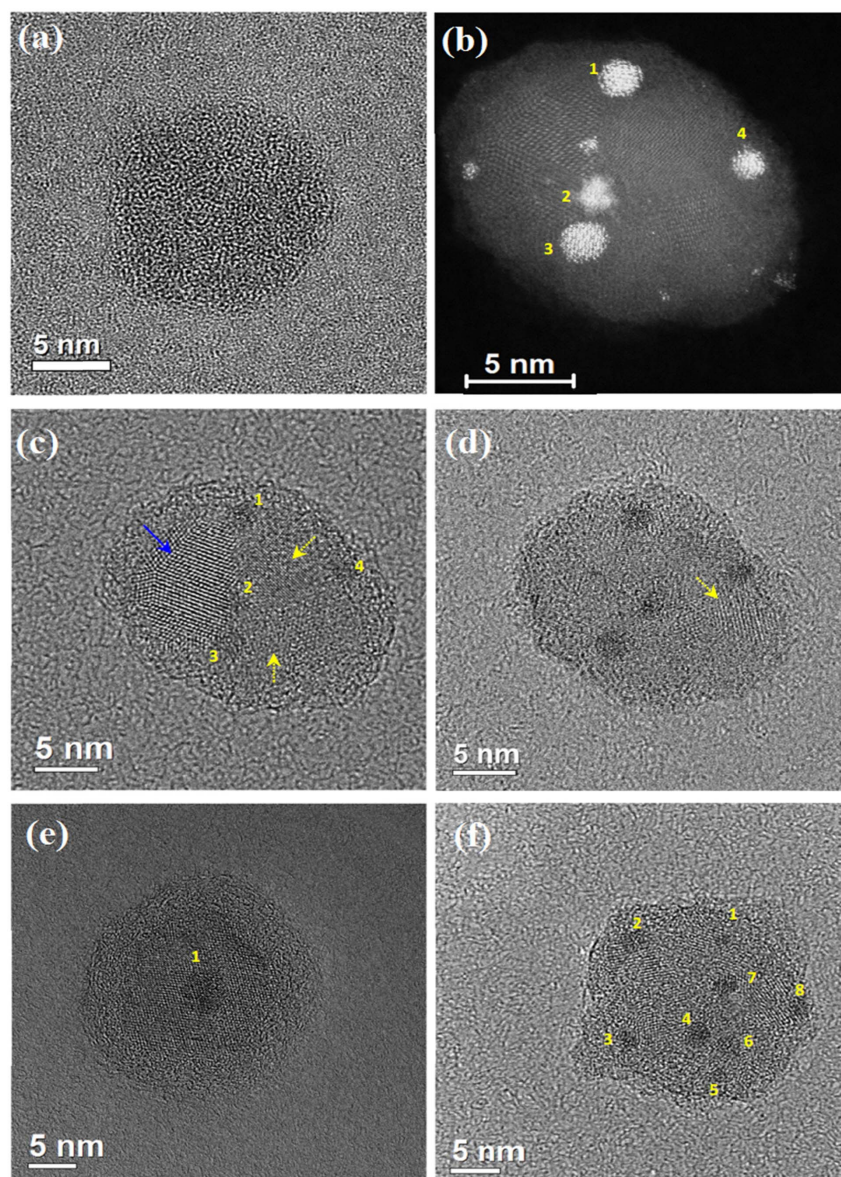


Figure 3 | HAADF-STEM and BF HRTEM micrographs showing the microstructure of uncoated and Ag-coated Si nanoparticles. Uncoated Si nanoparticles were amorphous, while Ag coated Si nanoparticles were nanocrystalline (a) TEM image of a control amorphous Si nanoparticle, without Ag coating. (b) HAADF-STEM image of coated Si nanoparticle decorated with several Ag nanoclusters (bright) marked by numbers 1–4 respectively. (c) TEM image of the same nanoparticle with unchanged orientation with respect to the electron beam. The Ag nanoclusters numbered 1–4 in HAADF mode image appear as dark spots in the corresponding bright field image. Qualitative correlation between the number of Ag nanoclusters on the surface and the number of grains in the Si core is evident in the BF HRTEM images of (c), four Ag nanoclusters and four Si grains; three grains are highlighted by arrows (one blue and two yellow) in (c) and a fourth grain was confirmed by tilting the sample by -15° relative to the incident electron beam as shown in (d). Further demonstration of the correlation is displayed in (e) and (f); with one Ag nanocluster marked by numeral 1 and one Si grain in (e), and eight nanoclusters marked by numeral 1–8 and a corresponding number of Si grains in (f), respectively.

clearly observed, which suggests a polyhedral structure³². Remarkably, as the number of Ag nanoclusters on the surface increases, the number of grains in the underlying Si nanoparticle also increases (Fig. 3c–3f). This is a novel finding, which offers the possibility of tuning the crystallinity of the Si core via inflight Ag decoration.

Control over the number of Ag nanoclusters decorating the Si cores. It was possible to control the number of Ag nanoclusters decorating the surface of the Si nanoparticles by adjusting the power supplied to the Ag magnetron sputter source. Low coverage was achieved at 60 W magnetron power, and coverage increased by increasing the power to 90 W and 120 W (Fig. 4a, 4b and 4c, respectively). In addition, it proved possible to selectively remove

the Ag nanoclusters via plasma etching of the sample, leaving the Si core, of desired crystallinity, intact (see BF-HRTEM image, Fig. 5a and HAADF-STEM image, Fig. 5b. Etch parameters are provided in the Methods).

MD computer simulations of Ag condensation on Si nanoparticles. Previously MD methods have been used to elucidate the formation process of simple single metal and semiconductor nanoclusters during inert gas condensation^{33–35}. However, the alloying behavior of two or more co-sputtered materials at the nanoscale remains largely unpredictable and hard to simulate. Atomic Ag–Ag and Si–Si interactions were modeled with the well-established Foiles EAM and Stillinger–Weber interatomic potentials, respectively^{36,37}. Ag–Si

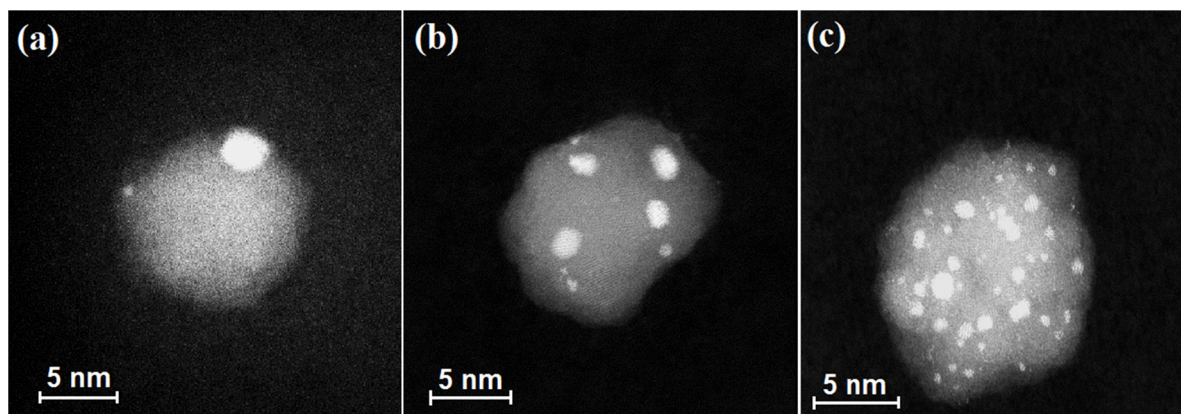


Figure 4 | HAADF-STEM micrographs demonstrating control over the number of Ag nanoclusters decorating the surfaces of the Si nanoparticles. Low coverage (d), medium coverage (e), and high coverage (f), obtained by applying 60 W, 90 W, and 120 W to the Ag magnetron sputter source, respectively.

mixed interaction was modeled with a pair potential based on a dimer potential calculated with a density-functional theory approach³⁸. Since potentials for gas phase dimers are known to overestimate the bond energy in the bulk, the obtained Ag-Si dimer potential was rescaled to provide an interaction that causes Ag and Si in the bulk to mix in the liquid phase, but segregate in the solid phase, as expected from the phase diagram³⁹. This behavior of the potential was checked with test simulations of initially liquid Ag and Si in a condensed system with periodic boundaries.

Actual condensation simulations were designed to correspond to the conditions in the Ag coating zone in the experimental setup (Fig. 1, labeled ‘II’). A pure Si nanoparticle of 1000 atoms was initially placed in the center of the simulation cell, and surrounded by a gas containing 243 Ag atoms that were initially isolated from each other, and were all outside the Si nanoparticle, (Supplementary Information, Movie S1). A snapshot at time $t = 0$ ns is shown in Fig. 6a. Computer resource limitations prevented simulation of larger Si nanoparticles, given the increased simulation duration (>50 ns) that would be needed to observe crystallization. The whole system was a cubic region with periodic boundary conditions and a side length that was varied between 10 nm and 80 nm, so as understand the pressure dependence of the results³³. For the Si nanoparticle that cools down by radiative cooling during flight⁴⁰, we initially set the system temperature to 3000 K. This is the temperature of the entire system, which comprises both the liquid phase of the Si nanoparticles and the vapor phase of Ag. Since these phases are weakly coupled, the temperatures of the nanoparticles and vapor may differ as the simulation proceeds; hence, the partial temperatures of Si and

Ag atoms were analyzed independently. The whole system was cooled down linearly to 300 K with cooling rates of 10 – 100 K/ns. Total simulation times were 0.1 – 0.3 μ s.

In the simulations, initially the system cooled from time 0 to 6.5 ns. At $t = 6.5$ ns and temperature $T_n = 825$ K a metastable phase transformation began with condensation of Ag atoms in the form of Ag nanoclusters on the surface of Si nanoparticles (Fig. 6b, Path P1). Ag vapor did not coalesce into nanoclusters in free space, but initially landed on the Si nanoparticle surface as discrete atoms, which nucleated to form nanoclusters (Fig. 6c). This was also confirmed experimentally by sputtering the Ag target under the same conditions without Si nanoparticles. No Ag nanoclusters were observed on substrates in the sample deposition chamber. Continuing with the simulations, from 6.5 to 20 ns, Ag nanoclusters grew due to subsequent deposition of Ag, and diffused into Si nanoparticles, forming locally Ag-rich liquid phases. At relatively low cooling rates (< 30 K/ns) and at $t = 10$ ns, the Ag-poor Si liquid phase solidified first (since undercooling of the Ag-poor Si liquid was higher than that of the Ag-rich liquid Si) and latent heat of fusion was released (Fig. 6b, path P2) reaching a maximum recalescence temperature of 1275 K. Subsequently, the fraction of disordered Si atoms (Fig. 6b, red curve) decreased to less than 10%. Directly within 10 ns of cooling along path P3 at $t = 20$ ns and $T = 965$ K, the Ag-rich Si phase solidified, forming a metastable Ag silicide (Fig. 6d). When the corresponding latent heat was released (Fig. 6b, path P4), a maximum recalescence temperature of ~ 1100 K (very close to the known Ag-Si eutectic temperature ~ 1118 K) was reached. The isothermal arrest, in combination with the still dynamic environment (ongoing Ag collisions

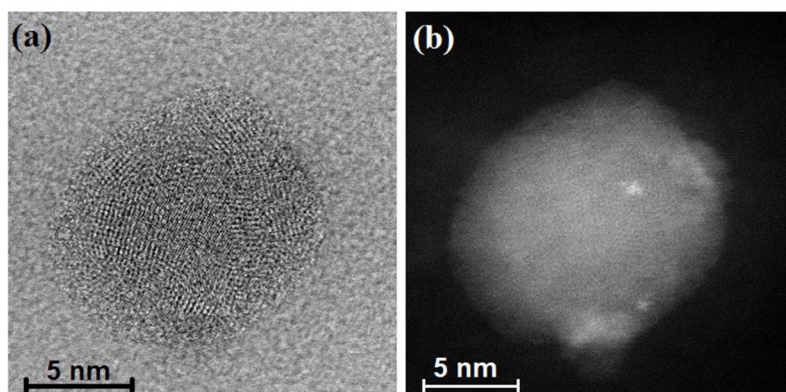


Figure 5 | Removal of Ag nanoclusters by plasma etching. (a) Bright field HRTEM and (b) HAADF-STEM images of a hybrid nanoparticle after plasma etching process. Ag nanoclusters on the surface were removed or reduced (compare with Figure 3) and the nanocrystalline Si core was left intact.

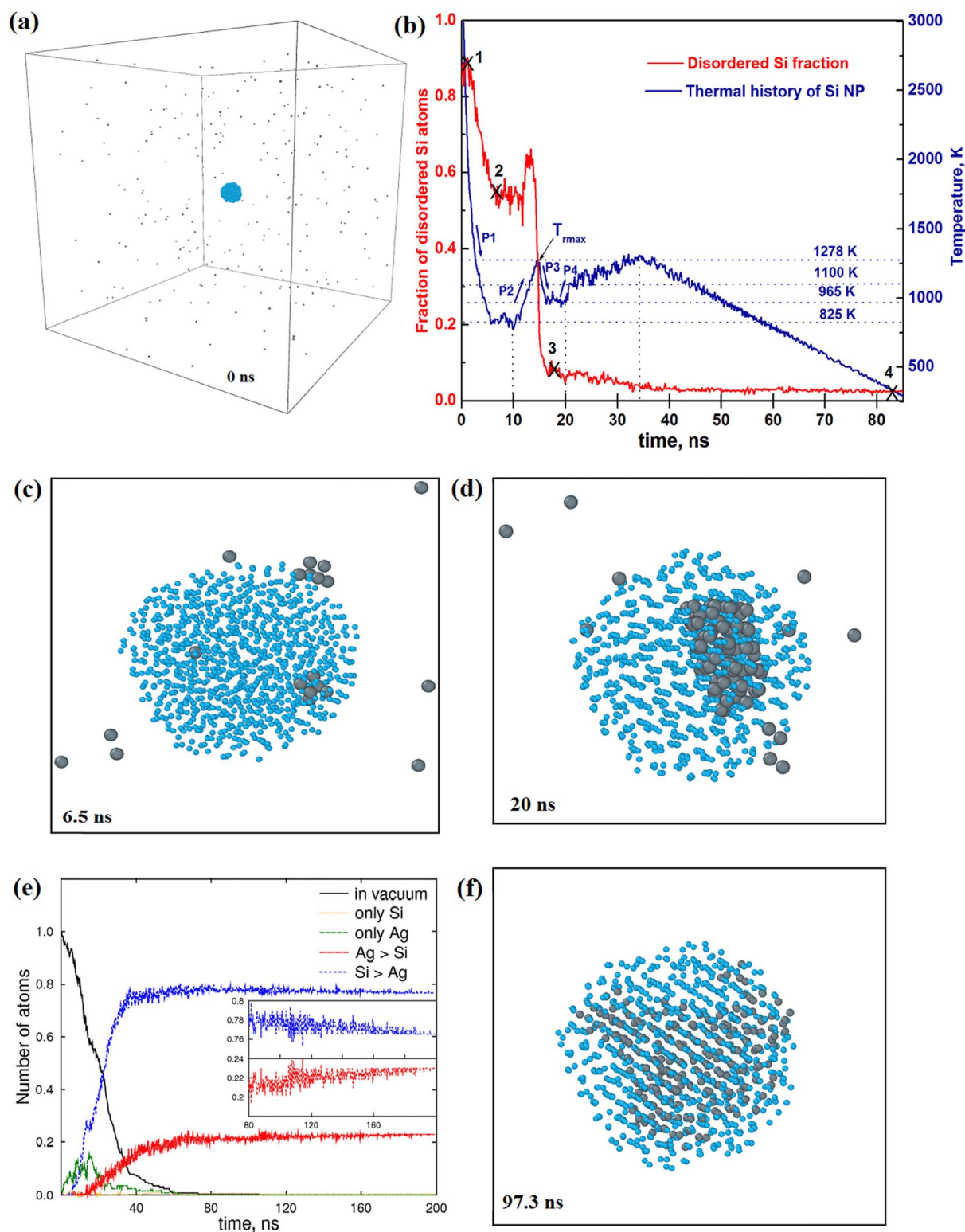


Figure 6 | MD computer simulations to model closely the Ag coating zone of the experimental setup (Figure 1, region ‘II’). Blue spheres correspond to positions of Si atoms and the gray spheres represent Ag atoms. (a) Initial state at 0 ns of a typical simulation cell, with 1000 atoms of pre-formed liquid Si nanoparticles in the center of the cell surrounded by a randomly dispersed Ag gas containing 243 atoms. Crystallization is quantitatively analyzed in (b), which shows the time development of temperature (in K) and the degree of disorder of the Si atoms in the Si nanoparticle, as measured by angular structure factor analysis. Times at which the snapshots (a), (c), (d) and (f) were taken are indicated by crosses and numerals (1–4) along the degree of disorder curve. (e) The local bonding environment of Ag atoms as a function of time. After crystallization, Ag showed a tendency to segregate, (see inset in (e)). The final state in the relatively short timeframe MD simulation (f), (coordinates taken at 97.3 ns) is a crystalline Si nanoparticle with Ag diffused into it. It is assumed that segregation would continue on timescales comparable to the experimental case. Considering that in a small nanoparticle some strain is always present, this may be considered to correspond to approximate perfect crystallinity.



with residual Ag atoms in the simulation cell) of the particle, explain the gradual rise in temperature from approximately $21 \text{ ns} < t < 35 \text{ ns}$. Toward the end of the simulation at room temperature, Ag can be expected to segregate out of the metastable silicide, which is consistent with the mutual immiscibility of Ag and Si in the solid state (Fig. 6e and 6f).

Discussion

The microstructural morphologies of the Ag-coated and uncoated Si nanoparticles (i.e. nanocrystalline and amorphous, respectively) suggests that the alloying behavior and phase dynamics during the coating process are more complex than simply attaching hetero-atoms to preformed nanoparticle seeds. The MD simulations employed explain the experimental observations. According to these simulations, the Ag atoms condense, nucleate and diffuse into the Si nanoparticles while still liquid, forming an intermediate alloying stage, and then segregate upon solidification. The post-deposition plasma etching provided an additional degree of freedom in nanoparticle design. One may retain the hybrid structure if it is advantageous to utilize combined properties of both the semiconductor core nanoparticle and the metallic nanoclusters decorating the surface for a given application, or one may selectively remove the metal nanoclusters, retaining only the intact Si core of desired crystallinity. In comparison to previously reported nanoparticles in the same application areas, this method offers the advantages of fabrication versatility, as well as the controlled size, structure and composition available from physical vapor deposition, in contrast to the chemical synthesis methods already reported^{23,25}. Furthermore, the well known problems of optical absorption and quenching by the metal shell can be elegantly sidestepped via the reported core-satellite structure²³. More generally, nanoparticle crystallinity control is a further advantage of our technique. The ability to explicitly and straightforwardly tune the atomic order from amorphous to polycrystalline to single crystalline offers tunability of the dependent optical, electrical and chemical properties, as well as a direct insight into the fundamental physical and chemical processes at work inside such nanoparticle systems^{41,42}.

In conclusion, we have devised a novel method to fabricate heterostructured Si–Ag nanoparticles with controlled microstructure and crystallinity based on inoculation of magnetron sputtered inert-gas aggregated Si nanoparticles, in flight, with Ag atoms. This method, coupled with the versatile and ubiquitous nature of sputter deposition technology provides a general method for the design and synthesis of novel, multicomponent, heterostructured nanoparticles with controlled crystallinity and microstructure for nanotechnology applications.

Methods

Materials. A silicon magnetron-sputtering target (Si n-type, purity >99.999%, resistivity $<0.001 \Omega\text{-m}$, dimensions: 25 mm diameter \times 3 mm thick) was purchased from Kurt J. Lesker (PA, USA). A custom-shaped silver magnetron sputtering target (Ag, purity >99.99%, resistivity $\sim 2 \times 10^{-8} \Omega\text{-m}$, dimensions: 150 mm length \times 50.8 mm width \times 3.0 mm thick) was purchased from K. Tech. Ltd. (UK). As substrates for AFM measurements, undoped Si dice with (100) orientation and 5 mm \times 5 mm in size were purchased from MTI Corporation (CA, USA). Carbon-coated grids (400 mesh) were purchased from Ted Pella Inc. (CA, USA), as substrates for TEM/STEM analysis.

Deposition conditions for amorphous–Si and Si–Ag heterostructured nanoparticles.

A UHV deposition system (Mantis Deposition Ltd, UK) was used for the production of the amorphous Si and nanocrystalline Si–Ag hybrid nanoparticles⁴³. The utilized Si sputtering conditions were Ar and He flow rates of 70 and 5 sccm, respectively (resulting in an aggregation zone pressure reading of 3.0×10^{-1} mbar); DC magnetron power of 90 W (18.3 W/cm²); and an aggregation zone length of 125 mm. These conditions were used for all synthesized Si nanoparticles. In the coating zone, Ag atoms were sputtered with an Ar gas flow of 10 sccm, whilst the DC magnetron power was varied over the range 60 W to 120 W (0.63 to 1.26 W/cm²) to explore the impact of Ag flux on the Si nanoparticles upon coating. Typical base pressures were 1.5×10^{-6} mbar adjacent to the aggregation zone and 8.0×10^{-8} mbar in the main deposition chamber.

Prior to deposition, silicon dice (for AFM images) were ultrasonicated in acetone, 2-propanol and deionized purified water (5 minutes each), and subsequently dried in a stream of high purity nitrogen. The cleaned Si dice surfaces exhibited a typical root-mean-square (rms) roughness of 0.17 nm. For TEM/STEM observations, nanoparticles were directly deposited onto carbon TEM grids in the UHV chamber. In the deposition chamber, substrate table rotation was set at 2 rpm for all depositions, to ensure good uniformity over the substrate area. Deposition time was 40 minutes in all cases, resulting in mono-dispersed particles. All depositions were performed at ambient temperature ($\sim 298 \text{ K}$, as measured by the substrate holder thermocouple).

AFM and TEM instrumentation and imaging. AFM was used for morphological characterization of the nanoparticles. A loadlock allowed sample transfer from the deposition UHV system, to an inert gas glovebox where AFM (Multimode 8, Bruker, CA) scans were performed under a controlled N₂ environment with ≤ 0.1 ppm oxygen level. The AFM was actively isolated using a vibration isolation table in order to minimize the noise level and guarantee the highest resolution performance. Scans were performed in soft tapping mode using commercial silicon-nitride triangular cantilever (spring constant 0.35 N/m, resonant frequency 65 kHz) tips with a typical radius $\leq 10 \text{ nm}$. The height distribution curves and rms roughness values were calculated from AFM images using the scanning probe image processor (SPIP) software (Image Metrology, Hørsholm, DK).

TEM studies were carried out using two 300 kV FEI Titan microscopes, equipped with spherical aberration correctors for the probe (for STEM imaging), and the image (for bright field TEM imaging), respectively. For the former, in TEM mode the spherical and chromatic aberrations were 1.2 mm and 1.6 mm, respectively. Point resolution was $\sim 0.20 \text{ nm}$, at Scherzer defocus conditions of -50 nm to $+60 \text{ nm}$. In STEM mode, the spherical aberration was in the range 0–5 μm , with chromatic aberration of 1.8–2.0 mm. Optimum HAADF–STEM resolution was approximately 0.1 nm. For the latter, an FEI Titan G2 Environmental TEM was used. In image-corrected TEM mode, the spherical and chromatic aberrations were $<5 \mu\text{m}$ and 1.4 mm, respectively, with an optimum resolution of better than 0.09 nm. In STEM mode, the spherical and chromatic aberrations were 1.2 mm and 1.4 mm, respectively, with optimum HAADF–STEM resolution of better than 0.136 nm. Energy dispersive x-ray spectroscopy (EDS) was performed with an Oxford X–max system, with an 80 mm² silicon drift detector (SDD) and energy resolution of 136 eV.

Plasma etching. Samples were plasma etched while mounted in the TEM holder, allowing TEM imaging of the same samples before and after the plasma exposure. A commercial plasma treatment system (Model 1020, E.A. Fischione, PA) was used to remove the Ag nanoclusters from the surface of the hybrid nanoparticles. The inductively-coupled plasma was created using a gas mixture of Ar and O₂, in the ratio 3 : 1, driven by a 13.56 MHz oscillating field system, resulting in expected ion energies less than 12 eV. Samples were etched for durations of 10 to 30 seconds.

- Xu, Y.-H. & Wang, J.-P. Direct Gas-Phase Synthesis of Heterostructured Nanoparticles through Phase Separation and Surface Segregation. *Adv. Matter.* **20**, 994–999 (2008).
- Fan, J. & Chu, P. K. Group IV Nanoparticles: Synthesis, Properties, and Biological Applications. *Small* **6**, 2080–2098 (2010).
- Yin, F., Wang, Z. W. & Palmer, R. E. Controlled Formation of Mass-Selected Cu–Au Core-Shell Cluster Beams. *J. Am. Chem. Soc.* **133**, 10325–10327 (2011).
- Lattuada, M. & Hatton, T. A. Synthesis, properties and applications of Janus nanoparticles. *Nano Today* **6**, 286–308 (2011).
- Peng, Z. & Yang, H. Synthesis and Oxygen Reduction Electrocatalytic Property of Pt-on-Pd Bimetallic Heteronanostructures. *J. Am. Chem. Soc.* **131**, 7542–7543 (2009).
- Alayoglu, S. & Eichhorn, B. Rh–Pt Bimetallic Catalysts: Synthesis, Characterization, and Catalysis of Core-Shell, Alloy, and Monometallic Nanoparticles. *J. Am. Chem. Soc.* **130**, 17479–17486 (2008).
- Ferrando, R., Jellinek, J. & Johnston, R. L. Nanoalloys: From Theory to Applications of Alloy Clusters and Nanoparticles. *Chem. Rev.* **108**, 846–872 (2008).
- Prodan, E. & Nordlander, P. Structural Tunability of the Plasmon Resonances in Metallic Nanoshells. *Nano Lett.* **3**, 543–547 (2003).
- Ferrer, D. *et al.* Three-Layer Core/Shell Structure in Au–Pd Bimetallic Nanoparticles. *Nano Lett.* **7**, 1701–1705 (2007).
- Habas, S. E., Lee, H., Radmilovic, V., Somorjai, G. A. & Yang, P. Shaping binary metal nanocrystals through epitaxial seeded growth. *Nature* **6**, 692–697 (2007).
- Tao, F. *et al.* Reaction-Driven Restructuring of Rh–Pd and Pt–Pd Core-Shell Nanoparticles. *Science* **322**, 932–934 (2008).
- Haberland, H. *et al.* Filling of micron-sized contact holes with copper by energetic impact. *Vac. Sci. Technol. A* **12**, 2925–2930 (1994).
- Bromann, K. *et al.* Controlled deposition of size-selected silver nanoclusters. *Science* **274**, 956–958 (1996).
- Palmer, R. E., Pratontep, S. & Boyen, H.-G. Nanostructured surfaces from size-selected clusters. *Nature Mater.* **2**, 443–448 (2003).
- Shyjumon, I. *et al.* Structural deformation, melting point and lattice parameter studies of size selected silver clusters. *Eur. Phys. J. D* **37**, 409–415 (2006).
- Kashtanov, P. V., Smirnov, B. M. & Hippler, R. Magnetron plasma and nanotechnology. *Physics Uspekhi* **50**, 455–488 (2007).



17. Li, Z. Y. *et al.* Three-dimensional atomic-scale structure of size-selected gold nanoclusters. *Nature* **451**, 46–48 (2008).
18. Mangolini, L., Thimsen, E. & Kortshagen, U. High-Yield Plasma Synthesis of Luminescent Silicon Nanocrystals. *Nano Lett.* **5**, 655–659 (2005).
19. Wang, J. *et al.* Surface plasmon resonance in interacting Si nanoparticle chains. *Nanoscale* **2**, 681–684 (2010).
20. Perraud, S. *et al.* Silicon nanocrystals: Novel synthesis routes for photovoltaic applications. *Phys. Status Solidi A* **210**, 649–657 (2013).
21. Olesinski, R. W., Gokhale, A. B. & Abbaschian, G. J. The Ag-Si (silver-silicon) system. *Bulletin of Alloy Phase Diagrams* **10**, 635–640 (1989).
22. Bokhonov, B. & Korchagin, M. In-situ investigation of the formation of eutectic alloys in the systems silicon–silver and silicon–copper. *Journal of Alloys and Compound* **335**, 149–156 (2002).
23. Jin, Y. & Gao, X. Plasmonic fluorescent quantum dots, *Nature Nanotechnology* **4**, 571–576 (2009).
24. Michalet, X. *et al.* Quantum Dots for Live Cells, in Vivo Imaging, and Diagnostics. *Science* **307**, 538–544 (2005).
25. Erogbogbo, F. *et al.* Plasmonic gold and luminescent silicon nanoplatforms for multimode imaging of cancer cells. *Integr. Biol.* **5**, 144–150 (2013).
26. Kalkman, J., Gersen, H., Kuipers, L. & Polman, A. Excitation of surface plasmons at a SiO₂/Ag interface by silicon quantum dots: Experiment and theory. *Phys. Rev. B* **73**, 075317 (2006).
27. Spinelli, P. *et al.* Plasmonic light trapping in thin film Si solar cells. *J. Opt.* **14**, 024002 (2012).
28. Mout, R., Moyano, D., Rana, S. & Rotello, V. Surface functionalization of nanoparticles for nanomedicine. *Chem. Soc. Rev.* **41**, 2539–2544 (2012).
29. Wang, Z. L. *Characterization of Nanophase Materials* (Wiley-VCH, New York, 2001).
30. Williams, D. B. & Carter, C. B. *Transmission Electron Microscopy: A Textbook for Materials Science* (Springer, 2nd ed., New York, 2009).
31. Hofmeister, H., Tan, G. L. & Dubiel, M. Shape and internal structure of silver nanoparticles embedded in glass. *J. Mater. Res.* **20**, 1551–1562 (2005).
32. Hofmeister, H., Dutta, J. & Hofmann, H. Atomic structure of amorphous nanosized silicon powders upon thermal treatment. *Phys. Rev. B* **54**, 2856–2862 (1996).
33. Allen, M. P. & Tildesley, D. J. *Computer Simulation of Liquids* (Oxford University Press, Oxford, England, 1989).
34. Kesälä, E., Kuronen, A. & Nordlund, K. Molecular dynamics simulation of pressure dependence of cluster growth in inert gas condensation. *Phys. Rev. B* **75**, 174121 (2007).
35. Harjunmaa, A. & Nordlund, K. Molecular dynamics simulations of Si/Ge cluster condensation. *Comput. Mater. Sci.* **47**, 456–459 (2009).
36. Foiles, S. M., Baskes, M. I. & Daw, M. S. Embedded-atom-method functions for the fcc metals Cu, Ag, Au, Ni, Pd, Pt, and their alloys. *Phys. Rev. B* **33**, 7983–7991 (1986). Erratum: *ibid.*, *Phys. Rev. B* **37**, 10378 (1988).
37. Stillinger, F. H. & Weber, T. A. Computer simulation of local order in condensed phases of silicon. *Phys. Rev. B* **31**, 5262–5271 (1985).
38. Nordlund, K., Runeberg, N. & Sundholm, D. Repulsive interatomic potentials calculated using Hartree-Fock and density-functional theory methods. *Nucl. Instr. Meth. Phys. Res. B* **132**, 45–54 (1997).
39. Tersoff, J. New empirical approach for the structure and energy of covalent systems. *Phys. Rev. B* **37**, 6991–7000 (1988).
40. Elihn, K., Landström, L. & Heszler, P. Emission spectroscopy of carbon-covered iron nanoparticles in different gas atmospheres. *Appl. Surf. Sci.* **186**, 573–577 (2002).
41. Mavros, M., Micha, D. A. & Kilin, D. S. Optical Properties of Doped Silicon Quantum Dots with Crystalline and Amorphous Structures. *J. Phys. Chem. C* **115**, 19529–19537 (2011).
42. Tang, Y. & Ouyang, M. Tailoring properties and functionalities of metal nanoparticles through crystallinity engineering. *Nature* **6**, 754–759 (2007).
43. Mantis Deposition Ltd. Retrieved 17th September 2013, from <http://www.mantisdeposition.com>

Acknowledgments

We thank Dr. Kouji Inoke from FEI Company (Tokyo, Japan) for assistance in TEM and STEM imaging.

Author contributions

C.C. deposited the nanoparticles and performed the TEM imaging. V.S. deposited the nanoparticles and performed the AFM measurements. F.D., K.N. and P.G. carried out the MD computer simulations. M.S. conceived the idea, designed the experiment, planned the experimental work and led the project. All authors contributed to writing and editing the manuscript.

Additional information

Supplementary information accompanies this paper at <http://www.nature.com/scientificreports>

Competing financial interests: The authors declare no competing financial interests.

How to cite this article: Cassidy, C. *et al.* Inoculation of Silicon Nanoparticles with Silver Atoms. *Sci. Rep.* **3**, 3083; DOI:10.1038/srep03083 (2013).



This work is licensed under a Creative Commons Attribution-NonCommercial-NoDerivs 3.0 Unported license. To view a copy of this license, visit <http://creativecommons.org/licenses/by-nc-nd/3.0>